This article was downloaded by: [National University of Ireland - Galway]
On: 14 September 2012, At: 00:54
Publisher: Taylor & Francis
Informa Ltd Registered in England and Wales Registered Number: 1072954 Registered office: Mortimer House, 37-41 Mortimer Street, London W1T 3JH, UK

Journal of Modern Optics
Publication details, including instructions for authors and subscription information:
http://www.tandfonline.com/loi/tmop20

Calibration and performance of a pyramid wavefront sensor for the eye

S. Chiesa [a] & J.C. Dainty [a]

[a] Applied Optics Group, School of Physics, National University of Ireland Galway, Galway, Ireland

Version of record first published: 10 Sep 2012.

To cite this article: S. Chiesa & J.C. Dainty (2012): Calibration and performance of a pyramid wavefront sensor for the eye, Journal of Modern Optics, DOI:10.1080/09500340.2012.717641

To link to this article: http://dx.doi.org/10.1080/09500340.2012.717641

PLEASE SCROLL DOWN FOR ARTICLE

Full terms and conditions of use: http://www.tandfonline.com/page/terms-and-conditions

This article may be used for research, teaching, and private study purposes. Any substantial or systematic reproduction, redistribution, reselling, loan, sub-licensing, systematic supply, or distribution in any form to anyone is expressly forbidden.

The publisher does not give any warranty express or implied or make any representation that the contents will be complete or accurate or up to date. The accuracy of any instructions, formulae, and drug doses should be independently verified with primary sources. The publisher shall not be liable for any loss, actions, claims, proceedings, demand, or costs or damages whatsoever or howsoever caused arising directly or indirectly in connection with or arising out of the use of this material.

Journal of Modern Optics
2012, 1–13, iFirst

Taylor & Francis
Taylor & Francis Group

Calibration and performance of a pyramid wavefront sensor for the eye

S. Chiesa* and J.C. Dainty

Applied Optics Group, School of Physics, National University of Ireland Galway, Galway, Ireland

(*Received 18 April 2012; final version received 27 July 2012*)

We describe the calibration and performance of a pyramid wavefront sensor designed for use in a retinal imaging camera. The effect of the image modulation and the sensor binning on the measurements are explained in detail and various tests to validate the performance are described. The wavefront sensor was incorporated into an adaptive optics system that used a magnetically actuated deformable mirror, and results on static test optics are shown.

Keywords: optical instrumentation and technology; vision science and applications; adaptive optics; wavefront sensing; retinal imaging

Downloaded by [National University of Ireland - Galway] at 00:54 14 September 2012

1. Introduction

Although Shack–Hartmann wavefront sensors are widely used today in ophthalmic research instruments, pyramid sensors have also been implemented for the eye. Iglesias and Ragazzoni [1,2] used the probe beam size at the retina to set the dynamic range and rotating diffusers to replace the mechanical modulation, and closed loop configuration using the conventional circular modulation scheme have been demonstrated [3–7]. The pyramid wavefront sensor has the advantage over the Shack–Hartmann in that the sensitivity and dynamic range are adjustable during its operation, permitting, for example, the sensitivity to be increased as an adaptive optics loop is closed. However, this advantage comes at the expense of greatly increased system complexity and cost.

In this work, we built a pyramid wavefront sensor for eventual use in an adaptive optics system for the eye. The issue of calibration raised for aberrometers based on Laser Ray Tracing [8], on Shack–Hartman [9] or on scanning Shack–Hartman [10] was similar for this adaptive optics system. Static calibration of the sensor signal and of the aberration reconstruction from the wavefront gradients ensured consistency with the direct observation of the single pass point spread function. The experimental measurement of the double pass ocular aberration using a narrow probe beam [11] was therefore validated. The ocular aberration corrected by the adaptive optics whose point spread function was observed at the imaging camera was thus quantified.

The first section is devoted to the description of the measurement system and of the calibration results acquired in response to a quantified aberration. Phase plates representing typical ocular aberrations were measured by the system so as to compare qualitatively the aberration measurement and the point spread function signal deterioration in the science path of the optical system. The adaptive optics efficiency was verified for these static aberrations.

The second section describes the measurement of the ocular aberration for five volunteers and its dynamic correction with adaptive optics using a high-stroke deformable mirror [12,13]. Simultaneous recording of the point spread function formed at the retina by the wavefront sensor laser beacon and of the ocular aberration measured by the sensor extended the calibration results to dynamic measurements.

The final section describes the fundus camera system incorporating the pyramid wavefront sensor. Calibration of the imaging system was performed in an artificial eye using reticle resolution targets, with the deformable mirror correcting for the optical system's aberrations.

2. Calibration of sensor response to an aberration

2.1. Sensor signal for circular modulation

If the modulation is represented as a tilt angle α applied along the vertical axis (Y) at the steering mirror, as in Figures 1 and 2, the focused beam is shifted by a value $R_{\mathrm{mod}} = f_1'.\ \tan\ \alpha$ at the pyramid. The more the incident beam position increases at the pyramid the stronger the deviation applied to the beam by the prism, thus the wavefront sensor camera pupil

*Corresponding author. Email: sabine.chiesa@gmail.com

ISSN 0950–0340 print/ISSN 1362–3044 online
© 2012 Taylor & Francis
http://dx.doi.org/10.1080/09500340.2012.717641
http://www.tandfonline.com

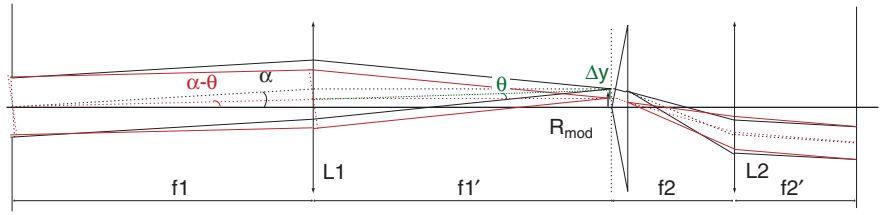

Figure 1. Modulation in telescopic arrangement for beam on pyramid upper facets. (The colour version of this figure is included in the online version of the journal.)

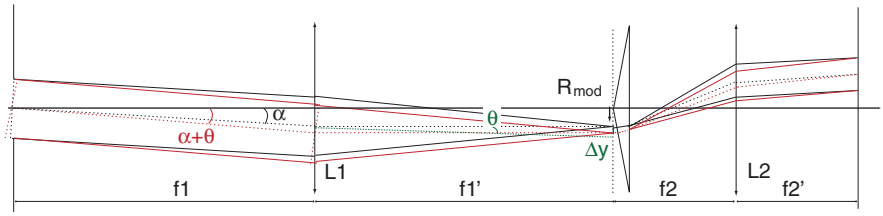

Figure 2. Modulation in telescopic arrangement for beam on pyramid lower facets. (The colour version of this figure is included in the online version of the journal.)

Downloaded by [National University of Ireland - Galway] at 00:54 14 September 2012

positions remain constant – until the modulation reaches the critical deviation angle for the prism. If the modulated beam at the steering mirror is tilted at an angle $+\theta$ towards the optical axis, the corresponding transverse aberration in the pyramid plane is a focus shift of $+\Delta y$. When the modulation projects the focus on the upper part of the pyramid, in Figure 1 for the angle $+\alpha$, the wavefront tilt and the modulation angle subtract, thus the focus is shifted by $-\Delta y$ in the pyramid plane.

When the modulation projects the focus to the lower part of the pyramid in Figure 2 for the angle $-\alpha$, the wavefront tilt and the modulation add, thus the focus is shifted by $-\Delta y$ in the pyramid plane. In consequence, the optical path becomes non-uniformly distributed amongst the four pyramid facets as in Figure 3(left). In the upper part of the prism the path b_1 is described by the angle ω defined by the modulation circle shift due to the transverse aberration Δ_y.

The signal at the wavefront sensing camera for the circular modulation of amplitude R_{mod} in the vertical direction s_y is given by the difference in the optical paths b_1 and b_2 traced by the shifted circle onto the pyramid top and down facets. The sensing signal s_y in the function of the transverse aberration Δ_y is written:

$$\frac{\Delta y}{R_{\mathrm{mod}}} = \sin\left(\frac{\pi}{2} S_y\right). \tag{1}$$

The horizontal gradient would be written similarly as in Equation (1) for a horizontal transverse aberration.

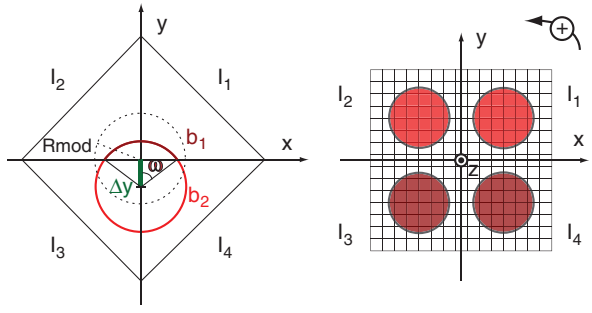

Figure 3. Modulation path, positive tilt of θ, adapted from [14]. The conjugated pupils at the camera plane receive more light in the direction containing the longest optical path, represented here by a brighter red shade in the top pupils. (The colour version of this figure is included in the online version of the journal.)

Any wavefront sample $W_P(x, y)$ of the pupil plane represents a horizontal and vertical gradient $(\partial/\partial i)$, with $i = x, y$ for the respective directions, described by the sensor signal $s_i(x', y')$ in the conjugated pupil plane:

$$\frac{\partial W_P(x,y)}{\partial i} = \frac{R_{\mathrm{mod}}}{f} \sin\left(\frac{\pi}{2} s_i(x', y')\right). \tag{2}$$

The sensor signal s_y is obtained by vertical differentiation of the detector pupil intensities $I_{i,(i=1,4)}$ for the pixel conjugated with $P(x, y)$ from the development of Equation (1):

$$s_y(x', y') = \frac{[I_1(x', y') + I_2(x', y')] - [I_3(x', y') + I_4(x', y')]}{I_1(x', y') + I_2(x', y') + I_3(x', y') + I_4(x', y')}. \tag{3}$$

Downloaded by [National University of Ireland - Galway] at 00:54 14 September 2012

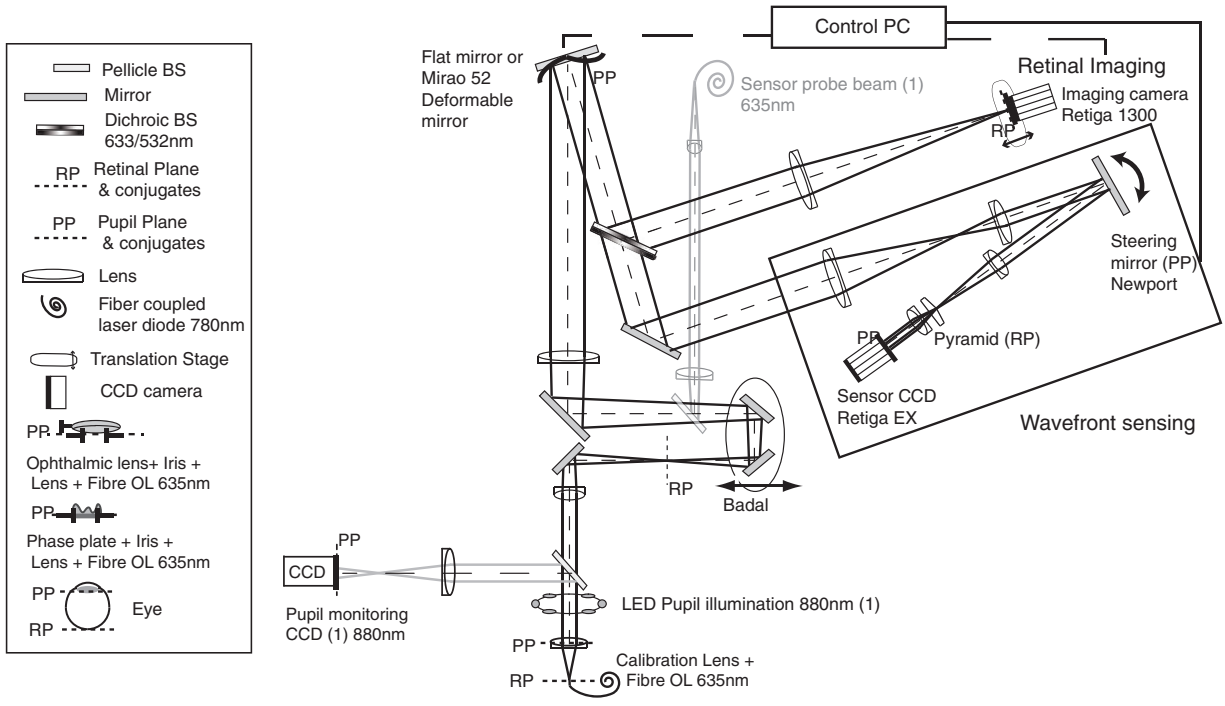

Figure 4. Schematic of optical bench used for calibration of sensor signal.

The expression is similar for a tilt in the horizontal direction with the horizontal wavefront gradient $\partial W(x,y)/\partial x$ with this time s_x:

$$s_x(x',y') = \frac{[I_1(x',y') + I_4(x',y')] - [I_2(x',y') + I_3(x',y')]}{I_1(x',y') + I_2(x',y') + I_3(x',y') + I_4(x',y')}. \tag{4}$$

Sensor saturation occurs when the signal $s_i(x',y')$ reaches ± 1, that is when the wavefront tilt displaces the signal onto only two facets of the prism. In that case the aberration Δy of Figure 3 is larger than the radius of modulation R_{mod}, and in turn the sensor detects a zero-signal in the top ($I_1 = 0$), ($I_2 = 0$) pupils and a maximal signal in the down pupils: ($I_3 = I_{\max}$), ($I_4 = I_{\max}$).

Hence:

$$\begin{aligned} s_x(x,y) &= \frac{[0 + I_{\max}] - [0 + I_{\max}]}{0 + 0 + I_{\max} + I_{\max}} = 0 \quad \text{and} \\ s_y(x,y) &= \frac{[0 + 0] - [I_{\max} + I_{\max}]}{0 + 0 + I_{\max} + I_{\max}} = -1. \end{aligned} \tag{5}$$

Equation (5) limits to $s_{xy} = [-1, 1]$ the range of values retrieved by the sensor, and means the saturation occurs when the range boundaries are reached.

2.2. System description

The system used for the calibration is presented in Figure 4.

The wavefront sensor calibration beam was defined at the pupil plane of the eye by a fibre laser source collimated by a 100 mm achromat lens and an iris aperture of 6 mm diameter. A telescope assembly conjugated the pupil plane to the deformable mirror Mirao 52-d (Imagine Eyes, France), through the Badal optometer mirror stage which was set at the mid-position of the translation range. A pellicle beamsplitter defined the input of the wavefront sensor probe beam focusing into the Badal stage. The pupil illumination optics was modified to perform measurements and closed loop, further described in Section 3. The magnified collimated calibration beam at the deformable mirror was reflected towards the wavefront sensor path. A second telescope assembly conjugated the pupil plane at the deformable mirror to the modulation control steering mirror. A dichroic beamsplitter (CVI Melles Griot) separated the wavefront sensing and retinal imaging paths. A last telescope assembly formed by a focusing lens and a re-imaging lens placed after the pyramid sensor relayed the steering mirror pupil plane to the wavefront sensor camera.

The circular modulation of the point spread function over the pyramid was provided in the pupil plane of the focusing lens by a steering mirror (Newport FSM-300). The surface deviation amplitude was determined by the voltages sent to the mirror amplifier by two synchronised function generators (Agilent 33250A

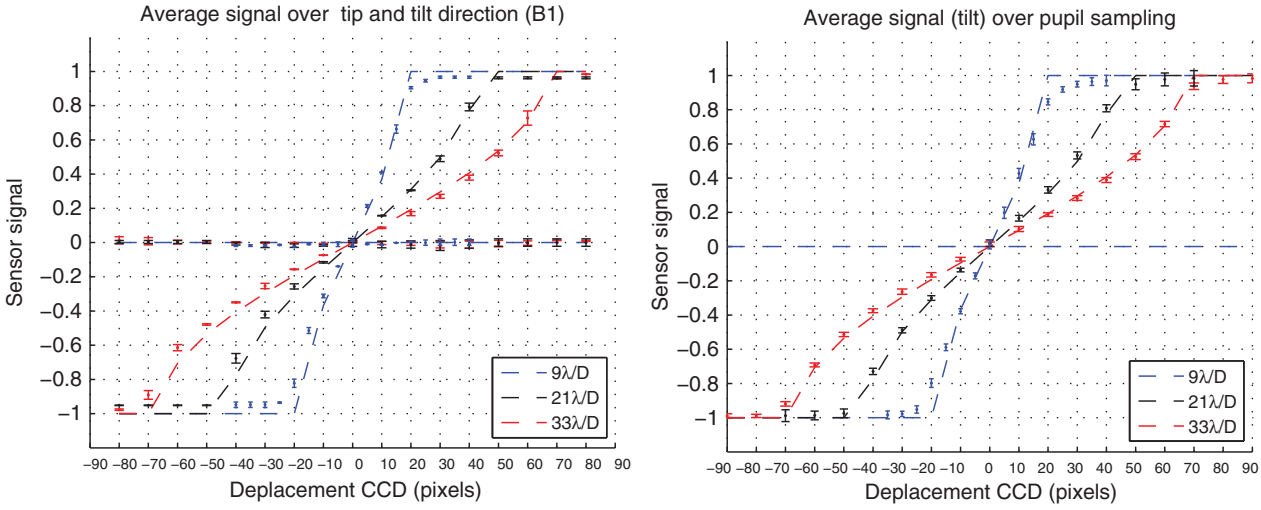

Figure 5. Sensor signal for modulation 9, 21 and 33 λ/D. Blue, red and black dashed lines model the sensor response for the tilt applied, and marks note the average value measured over the sensor signal. Error bars are the standard error of the mean for one frame in each direction in (left) and for one frame in each binning in (right). (The colour version of this figure is included in the online version of the journal.)

and 33120A), and was limited by a cut-off frequency above which the mirror response was attenuated.

Acquisition of the sensor signal, of the science camera and control of the adaptive optics was performed with a single desktop PC (Dell Omniplex 745). For a given wavefront measurement, the science camera frame and mirror surface deflection amplitudes were also recorded within a time lag of the order of a millisecond. The root-mean-square (rms) calculated from the sensor measurement for a given science image defined a criterion for the alignment of the system.

Illumination of the pupil of the eye was provided by an assembly of 880 nm infrared LEDs mounted in a ring. The pupil axial position was determined when the iris of the eye was in focus on the pupil camera monitor. The pupil image was captured by an infrared CCD (Thomson, 640×480 pixels) then transferred via a frame-grabber to a separate PC operating system. This light source was switched off during the wavefront sensor signal and retinal image acquisition to avoid the presence of an additional source of background light for the wavefront sensor. The pupil monitoring was based on the back-reflection of the probe beam from the retina out of the eye.

2.3. *Tip and tilt in the sensor signal*

When the fibre laser mount was shifted in the back focal plane of the collimation lens in the calibration arm, the transverse shift of the point spread function at the science camera (measured in pixels from the central position) corresponded to the tilt introduced in the pupil plane at the edges of the calibration iris. From the minimum modulation radius defined by the radius of the Airy function to the maximal modulation amplitude defined by the steering mirror cut-off for 100 Hz signals, the sensor sensitivity adjustment corresponded to factors M1 to M14. The modulation factors Mi ($i = 3$, 7, 11) represent, in Figure 5, three values evenly distributed (M3 = 9 λ/D, M7 = 21 λ/D and M11 = 33 λ/D) in the full range of modulations applied.

The comparison of the computed sensor signal with the experimental signal recorded over the tip and tilt directions is presented in Figure 5(left). The amplitude of the standard error of the mean shows that the sensor response is consistent with the theory in both directions of tilt. The same measurement performed over a single direction (tilt) but with a variable number of samples in the pupil is presented in Figure 5(right). The amplitude of the standard error of the mean shows the measured signal is consistent with the theory for all the pupil sampling configurations. In both cases the experimental data and the model are in excellent agreement. From Figure 5, the maximal extension of sensing range is, in pixels, nine times larger than the minimum sensor range.

3. Application to the measurement of ocular aberration

Wavefront measurements were expressed in metric units (μm), quantifying the wavefront departure from the reference sphere as the root-mean-square (rms)

Downloaded by [National University of Ireland - Galway] at 00:54 14 September 2012

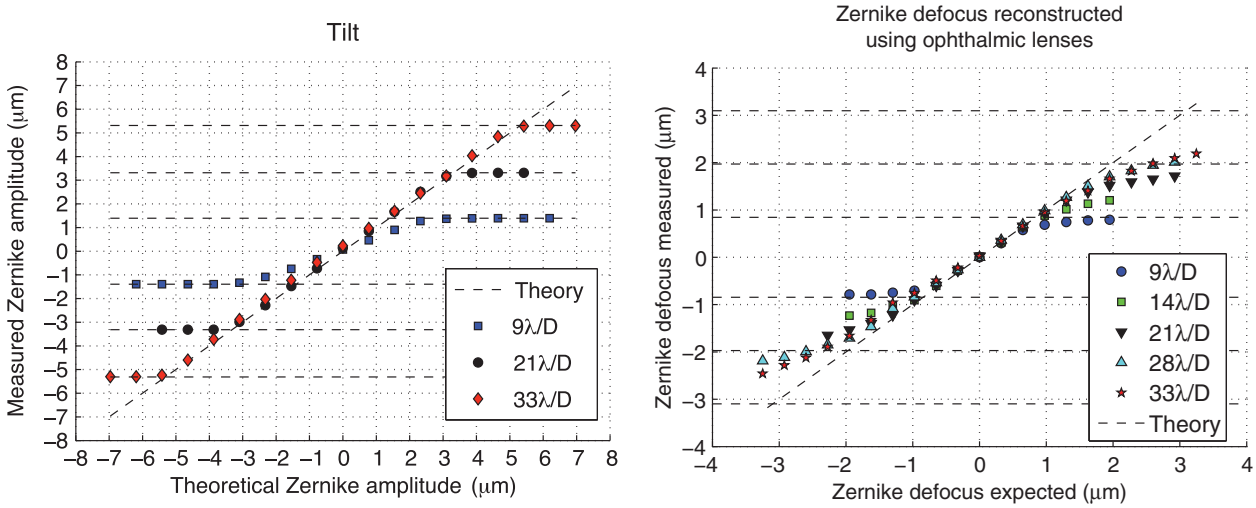

Figure 6. Tilt and defocus measured at the highest pupil sampling (B1, 109 μm per sample). Horizontal dashed lines show the saturation limits of the Zernike term for each dynamic range defined by the modulation factors 9, 21 and 33 λ/D. Linearity of the sensor response is satisfied when the theoretical and measured term amplitudes correspond. Sensor saturation for defocus is reached at $9\lambda/D$. (The colour version of this figure is included in the online version of the journal.)

Downloaded by [National University of Ireland - Galway] at 00:54 14 September 2012

wavefront error. The aberrations were expressed in the single-indexing notation of normalised coefficients from the Zernike circular polynomials [15–17]. Pupil size was fixed by the detection software and the reconstruction was centred on the pupil.

In ocular measurements, tip and tilt coefficients ($j=1$, $j=2$) were included in the rms calculation then displayed separately from the higher-order terms. The error in a Zernike term for the mean value presented was defined by the standard deviation of the mean of the term for a series of static measurements. This variation was very low for the calibration compared to the measurement of the dynamic ocular aberration.

3.1. *Tip/tilt, defocus and higher-order aberrations*

In both Figure 6 (left) and (right), the wavefront aberration presented was experimentally determined after the average reconstruction over five single sensor acquisitions. The Zernike tilt term was obtained from the sensor signal recorded after transverse displacement (tilt) of the fibre output at the back focal plane of the calibration lens as in Section 2.3 in steps of 30 pixels at the retinal imaging camera. Zernike defocus was tested using ophthalmic lenses of ±1.5 D sphere power in steps of ±0.5 D.

The theoretical Zernike tilt signal was modelled using geometrical optics to relate the lateral displacement of the point spread function at the science camera to the angular tilt at the pupil plane of the calibration arm and scaling for the pupil diameter to obtain the aberration in micrometers. Theoretical defocus amplitude was modelled using the conversion equations [18] from the refractive power of an ophthalmic lens into Zernike decomposition.

The standard deviations of the mean for each point was of the order of 10^{-3} μm, thus the measurement stability was verified for such static aberration. Sensor saturation at a given dynamic range corresponded to a constant value of the aberration. Sensor nonlinearity was represented by the departure of the measurement from the theoretical value. The tip-tilt nonlinearity range coincided with the saturation range while the defocus nonlinearity spread over a wider range of aberrations before the saturation value.

The static response of the system to typical ocular aberrations was measured by placing in the pupil plane of the calibration arm, plastic plates engineered with a resin substrate deposited in the shape of a known phase aberration [19]. Plate 1 and plate 2 were shaped as typical ocular aberrations of human eyes. Plate 3 and plate 4 were shaped in a known amplitude of known aberration, defocus (Z20) and trefoil (Z16).

The plates' wavefront aberration was first measured using a Twyman–Green interferometer (Fisba Optik, Switzerland) which provided high-resolution surface characterisation of the patterns with 10 μm per wavefront sample over the 6 mm measurement pupil. The plates were then positioned individually in the pupil plane of the calibration beam and the phase was measured at each of the four sensor sampling settings for the three test modulations. For each pupil sampling setting, 50 sensor measurements of the aberration were acquired and the respective wavefronts reconstructed. A 10^{-3} μm rms variability of the rms error over the

Downloaded by [National University of Ireland - Galway] at 00:54 14 September 2012

50 frames confirmed the stability of the sensor measurement for each pupil sampling. The aberration coefficients averaged over the sampling setting for each dynamic range for each phase plate are displayed in Figure 7 with the wavefront decompositions fitted from the interferometer measurement. The average wavefront rms for all dynamic ranges compared to the rms of the plate measured by the interferometer is presented in the title of the displays in Figure 7. Detailed values of rms for each dynamic range averaged over the binning are presented in Table 1.

For low-order modes (defocus Z4, astigmatism Z3 and Z5) a higher coefficient variability with the pupil sampling was observed than for the higher orders. As the pyramid is considered as an appropriate sensor for these modes, this effect could be related to the change in the pupil sampling. Additional astigmatism in the pyramid measurement in plate 1 and 3 and defocus, and secondary astigmatism in plate 4 decreased the fit between the two measurement systems. These were attributed to the slight changes in the plate's lateral positioning, pupil size and reference wavefronts in the respective setups [20].

An average rms variability of $\pm 0.03\,\mu m$ with the pupil sampling was obtained for the aberration measurement by the sensor. The sensor pupil sampling change was thus not negligible in the measurement of an aberration. The number of pupil sampling sets tested here (four) was not sufficient to determine a trend. An average variability of $\pm 0.04\,\mu m$ with the dynamic range was obtained for the aberration measurement by the sensor. This confirmed the influence of the sensor dynamic range on the aberration measurement. The average rms measured by the sensor for each plate was $0.1\,\mu m$ higher than the interferometer rms, which represented the differences in positioning of the plate in the pupil plane and the differences between the sensor settings and the interferometer settings. The suitability of the pyramid system built for these ranges of aberrations was confirmed by comparison of the aberration amplitudes measured with the calibration curves for defocus in Figure 6. The phase plate aberrations were well below the sensor limits for the modulation considered.

3.2. Ocular aberration measurement

The eye was dilated using a drop of Tropicamide 1% ophthalmic drug. Once the accommodation was frozen the subject's head was aligned through positioning of the bite bar mount installed on a three-axis translation stage itself fixed to the optical bench, which fixed its position relative to the optical axis of the system. Sequences of 5 seconds of open loop measurement and 5 seconds of closed loop measurement were recorded for three values of the modulation factor within the sensor maximal and minimal modulation range. The rms traces over time were initially calculated including all the terms of the Zernike decomposition – that is, also with tip and tilt. These data for the four subjects are presented in the upper part of Figure 8. In the average Zernike decomposition over 10 frames in open loop the tip and tilt amplitudes were identified at their saturation values and thus as taking over on all other terms in the rms traces. The tip and tilt amplitudes are respectively presented in the lower part of Figure 8. In the eye the adaptive optics was recorded without changing this camera position. The assumption was that the adaptive optics system was taking the highest level of intensity to calculate the correction, and bring the focus to the corresponding layer of the retina. The point spread function images for the four subjects are presented in Figure 9. The first two subjects S1 and S2 were imaged using a 16 bit depth science camera image at the highest camera image resolution at 50 ms and 20 ms exposure and default camera gain (1016/4095 arbitrary units), while subjects S4 and S5 were imaged using an 8 bit image depth, the highest camera resolution and 5 ms exposure camera.

3.3. Discussion

Given the amplitude of the error bars in the data of Figure 8, the assumption that the sensitivity range evolution is of benefit for the measurement of a given azimuthal order of aberrations cannot be verified. For the low speed of the acquisition system with typically 5–10 Hz for the 56 samples across the pupil (each sample measuring $107\,\mu m$ at the eye), it is likely that the temporal variations of an order would introduce errors in the characterisation.

For the aberrations measured with tip and tilt saturation amplitudes, the Zernike decomposition was thus not properly characterised. The closed loop amplitude of a Zernike term was defined as the noise level for this term at the modulation amplitude considered. The difference between the higher-order term amplitude before and after closed loop was however too small to identify if the maximal wavefront aberration had been reached for this order. With only three modulations factors tested it is possible that the best sampling dynamic range for the aberration would not appear. The wavefront tip and tilt amplitudes were determined by the position of the probe beam on the retina from the closed loop reference, thus the pre-correction of the beam position should have been applied. Instead of maintaining the same probe beam orientation for all subjects, a customised adjustment of

Downloaded by [National University of Ireland - Galway] at 00:54 14 September 2012

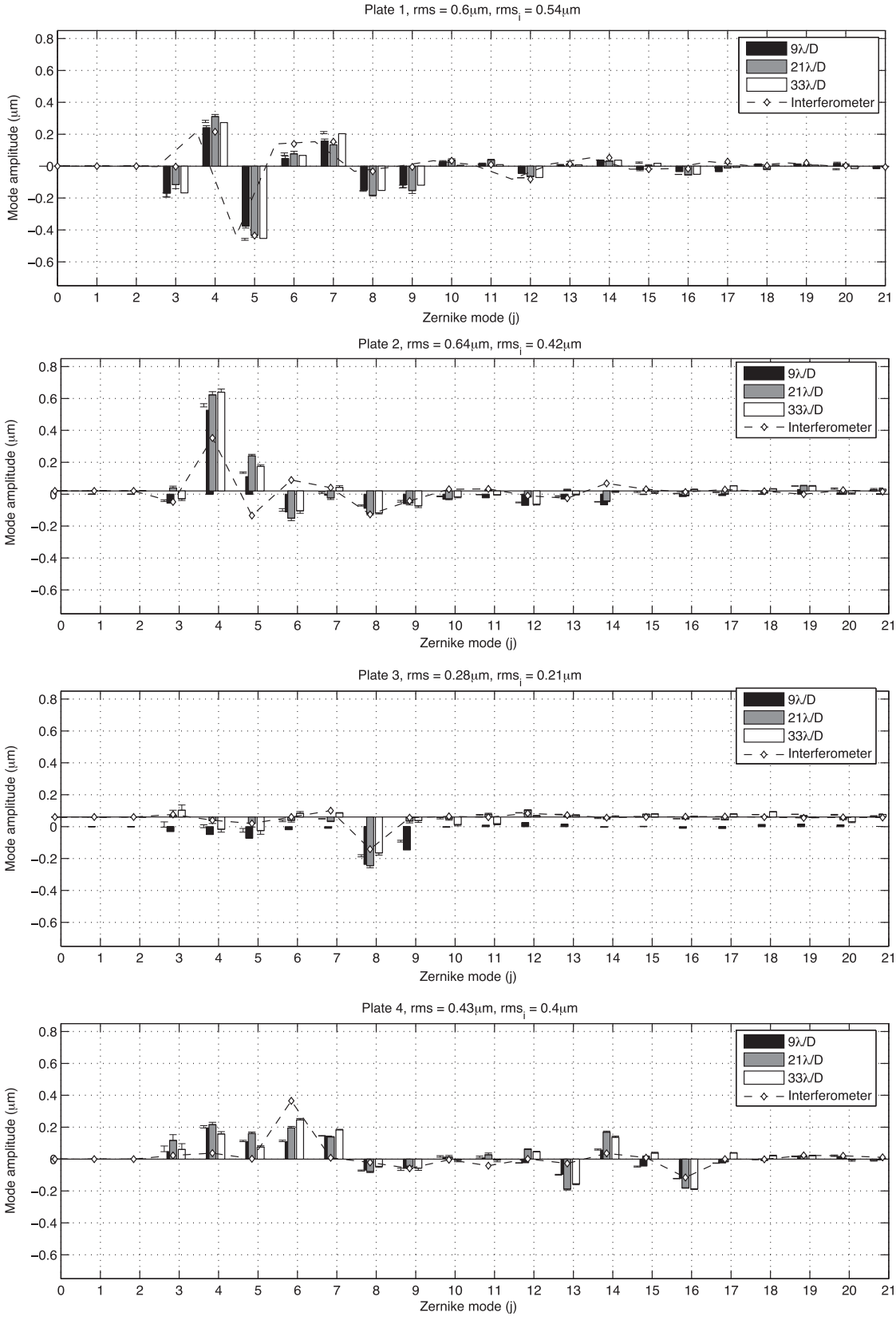

Figure 7. Zernike phase plate coefficients after wavefront reconstruction. Dashed line with diamond mark is the interferometer measurement; black, grey, and white bars show 9, 21 and 33 λ/D modulation. rms is calculated from the coefficients' root-mean-squared error of the sensor wavefront measurement averaged over the three modulations and rms_I is calculated from the interferometer single measurement. Error bars are the standard error of the mean over the four pupil samplings.

Table 1. RMS of phase plates measured at modulation factors 9, 21, 33 λ/D and with a Fisba interferometer. Standard deviation of each rms corresponds to the variation over the pupil sampling setting.

rms (μm)	Plate 1	Plate 2	Plate 3	Plate 4
Interferometer	0.54	0.42	0.21	0.40
M3 = 9 λ/D	0.55 ± 0.01	0.57 ± 0.02	0.30 ± 0.01	0.35 ± 0.01
M7 = 21 λ/D	0.63 ± 0.01	0.69 ± 0.07	0.32 ± 0.03	0.50 ± 0.02
M11 = 33 λ/D	0.63 ± 0.06	0.68 ± 0.05	0.28 ± 0.01	0.47 ± 0.03
Mean (all M)	0.60 ± 0.04	0.65 ± 0.05	0.30 ± 0.02	0.44 ± 0.06

Downloaded by [National University of Ireland - Galway] at 00:54 14 September 2012

the probe beam direction in the pupil and position at the pupil should have been performed by adjustment of the transverse controls of the probe beam assembly.

Thanks to the deformable mirror stroke amplitude, the sensor saturation did not stop the adaptive optics operating. The lack of saturation detection did not represent a problem for the adaptive optics given that the high stroke of the mirror corrected most of aberrations. However, the experimental parameter adjustment required to obtain a proper ocular aberration quantification was not performed before the closed loop was started, and secondly the closed loop sometimes revealed instabilities.

The lower signal to noise ratio observed in the point spread function of subject S5 was attributed to his darker eye colour compared to the three other subjects as the laser power was set constant at 2.5 μW power. All images show a 48×48 arcmin field in the eye using a higher zoom factor for the subjects S4 and S5. The shift between the open loop position and the closed loop position pointed by a centroid identification algorithm applied to the point spread functions was of similar amplitude for all the subjects and of 12.6 arcmin (63×63 μm for an eye length of 17 mm). This a constant shift represented the constant laser position and an angular shift and was consistent with the global tip/tilt measured for all the subjects in Figure 8.

In conclusion, the saturation of the sensor due to tip and tilt was identified after reconstruction of the wavefront decomposed into Zernike coefficients from the sensor data. The ocular aberration correction was still achieved by the adaptive optics system from the mirror surface deflection defined by the adaptive optics mirror voltages. A 0.1 μm root-mean-squared wavefront error amplitude was identified to a characteristic shape of corrected point spread function observed for all five subjects. The second probe beam system was designed so that the tip and tilt could be readjusted on the retina manually. The incoming probe beam defocus could not be controlled. The aberration correction was then limited to the higher-order terms.

4. Calibration of imaging system and application to a model eye

This section describes the imaging system resolution for a model eye and the implementation of illumination optics. After correction of the optical system's aberrations, imaging of a resolution target defined the experimental magnification.

4.1. Retinal image resolution in model eye

A first optical relay formed by the first lens of focal length $f' = 125$ mm after the eye and the lens of the eye created a conjugate retinal plane in the system before the Badal optometer. For an Emsley reduced model eye of length $l = 22.2$ mm and modelled vitreous refractive index $n = 1.33$, the equivalent focal length in air is $f' = 16.7$ mm. For a 6 mm diameter eye pupil in the green ($\lambda = 540$ nm), an object of size below 3 μm cannot be imaged by the system. For the imaging system, geometrical optics defined that a camera pixel of 6.45 μm side covered in the model eye retinal plane a squared area of 0.86 μm side. A feature of 3 μm represented 3.5 pixels of the image, thus the Nyquist criterion was satisfied.

4.2. Retinal illumination

The illumination path design presented in Figure 10 is implemented in place of the pupil monitoring system of Figure 4. The optical design is similar to the Köhler system used in microscopy, using the conjugation of the LED source (Philips Luxeon V star) to the cornea to illuminate the retina in Maxwellian view. An iris in a conjugate plane defines the retinal extent of the illumination at the retina, and a custom-designed fixation target printed onto a transparent plate defines the retinal extent imaged at the camera.

Lens arrangements (L_1, L_2) and (L_3, L_4) have equivalent focal lengths f'_{eq0} and f'_{eq}, and the eye is approximated by a sphere of refractive index n. The field iris defines the angular illumination at the retina. The fixation target defines the position imaged in the

Downloaded by [National University of Ireland - Galway] at 00:54 14 September 2012

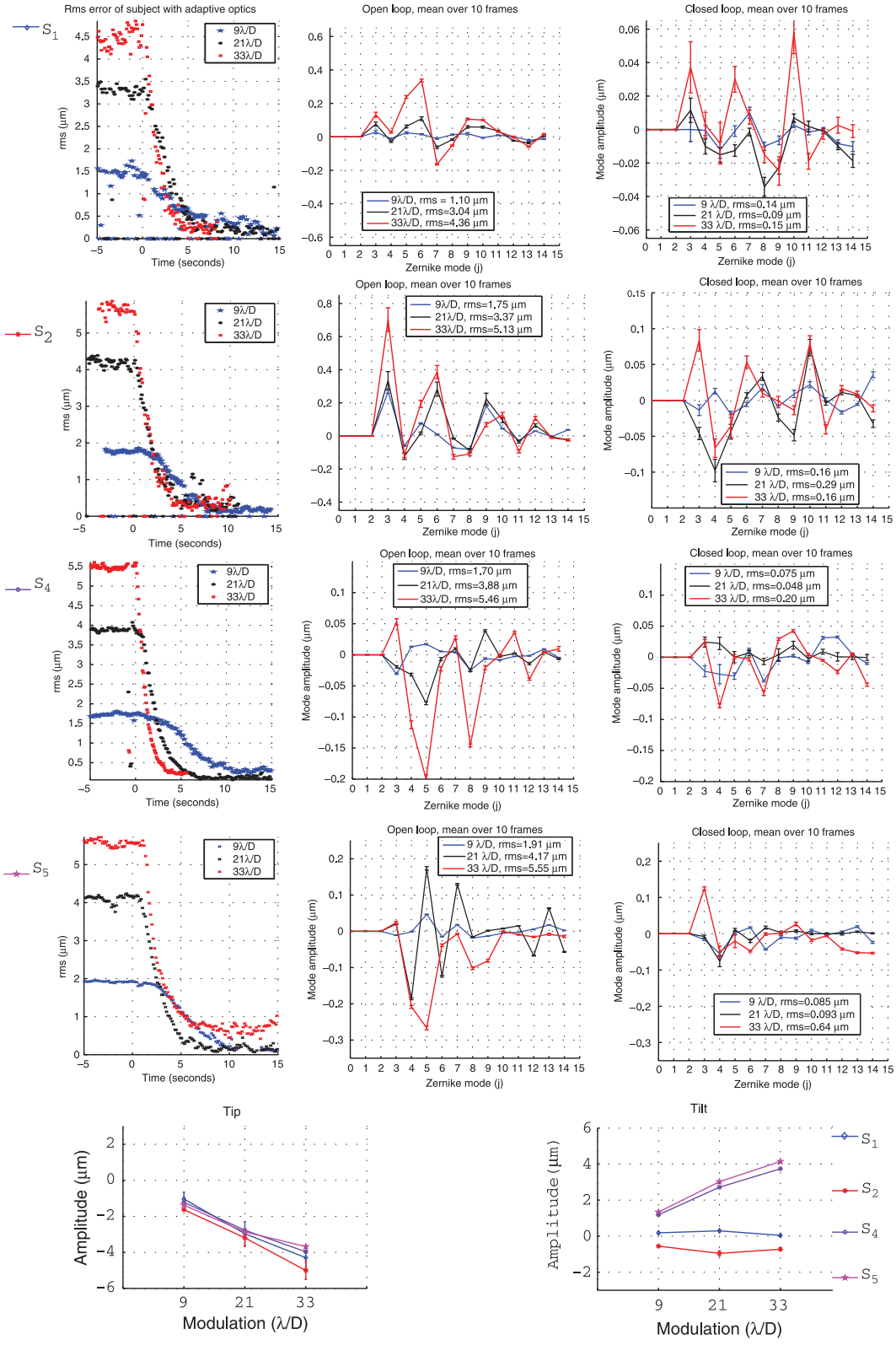

Figure 8. Column 1: rms error over time. Column 2: open loop Zernike decomposition for four subjects. Column 3: closed loop decomposition for four subjects. Each order of the decomposition corresponds to a 10-frame average taken within the rms in open loop and in closed loop for Column 1. Tip and tilt amplitudes for open loop in each modulation factor are presented in the lower part for each subject $S_{1,\ldots,4}$. Tip–tilt saturation amplitudes for 9, 21 and 33 λ/D are, respectively, |1.4|, |3.4| and |5.3| μm. (The colour version of this figure is included in the online version of the journal.)

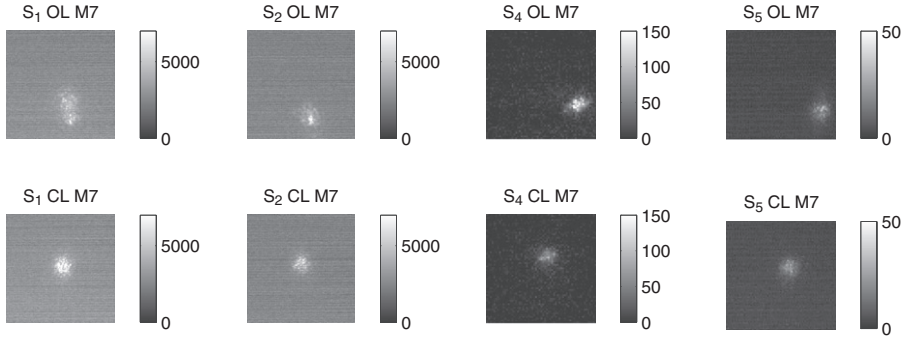

Figure 9. Point spread function displacement for the four subjects without adaptive optics (OL) and with adaptive optics (CL). The lateral shift of the double pass closed loop measured with a centroid algorithm corresponds to tip and tilt amplitudes leading to wavefront sensor saturation. Closed loop signal diameter measured with a centroiding algorithm of 40 μm (≃8 arcmin).

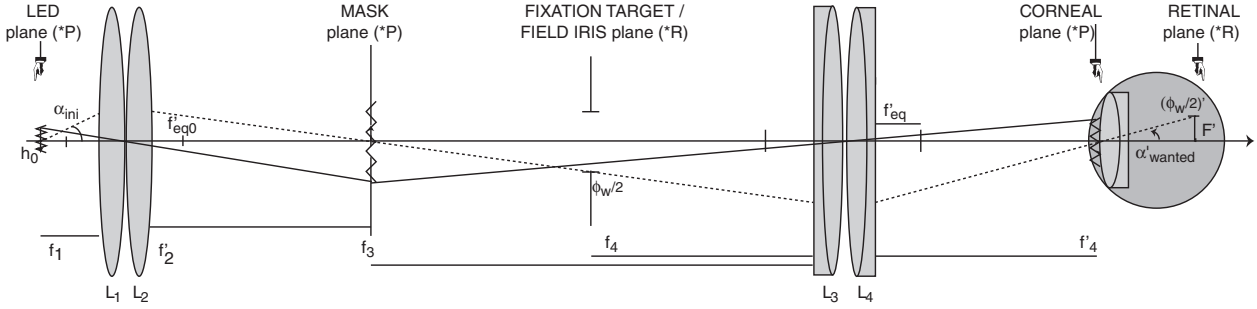

Figure 10. Schematic illustration of the illumination system designed using geometrical optics. First relay of the LED is based on singlets as the intensity transmission is the main concern while second relay is based on doublets for better viewing of the fixation target.

retina. The mask external radius h_{ext} is re-imaged into a mask image of external radius h'_{ext} at the cornea. The field iris aperture size Φ_w and output divergence angle α_{wanted} sets the size and divergence Φ'_w and α'_{wanted} of the illumination at the retina.

4.3. Imaging of USAF target

Replacing the eye by an assembly based on a 16 mm lens and USAF 1951 resolution target (Edmund Optics MIL-S-150A, positive) enabled the system resolution to be estimated with the adaptive optics correcting for the system's aberrations. A pixel of the camera at the artificial eye represented 0.82 μm of the resolution target. The Nyquist criterion states the resolution limit of the object at 1.64 μm spread onto two pixels of the detector. In Figure 11 the smallest bars are in Group 7, Element 6 of spacing frequency 228 cycles/mm defined by a black line and a white line pattern of 4 μm width and largest pattern belong to Group 6 Element 1 (64 cycles/mm, 15 μm width). The image cross-sections plotted along the rows marked by the arrows show the contrast decrease with the increase in spatial frequency of the pattern. Contrast for the bars of spatial frequency 228 cycles/mm is ≈30% while contrast for spatial frequency of 72 cycles/mm is ≈80%. With five pixels describing the highest frequency pattern, using 2.5 pixels to reproduce the bar edge, the resolution limit of the system predicted is verified.

4.4. Imaging of static structure

Further testing of the imaging with adaptive optics was performed with an artificial eye based on a soft plastic ball of 30 mm diameter ('RUBR-EYE'). Correction of the aberration by the deformable mirror was necessary to form an image of the inside of the structure. Calibration of the magnification between the back of the structure after correction was performed using the system described in Figure 4 and a dual crosshair reticle (Linos Qioptic 5×7.5 mm, 10 μm) positioned behind the RUBR-EYE. An image acquired at 100 ms at 540 nm with the flashed illumination using adaptive optics with 110 μm per pupil sample and the dynamic range corresponding to $21\lambda/D$ is presented in Figure 12(left). From the distance between the

Downloaded by [National University of Ireland - Galway] at 00:54 14 September 2012

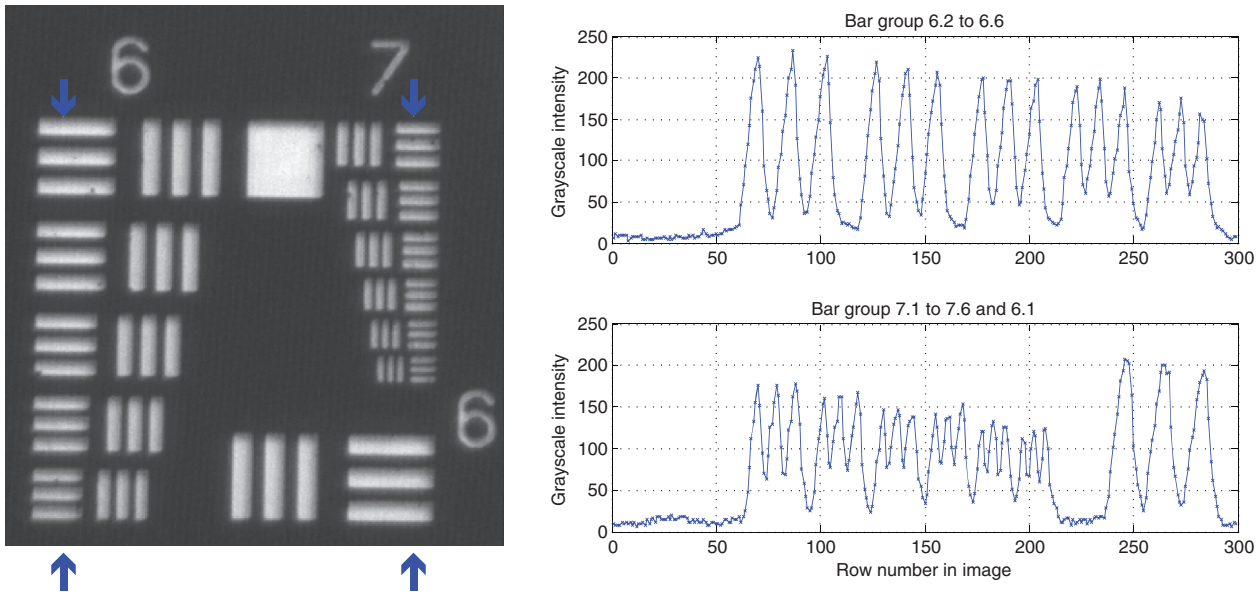

Figure 11. US Air Force resolution target on glass substrate imaged at highest resolution setting with flashing system at 10 ms, 8-bit image (left). Image intensity cross-sections along the rows pointed to by the arrows are displayed in the upper-right and lower-right plots. (The colour version of this figure is included in the online version of the journal.)

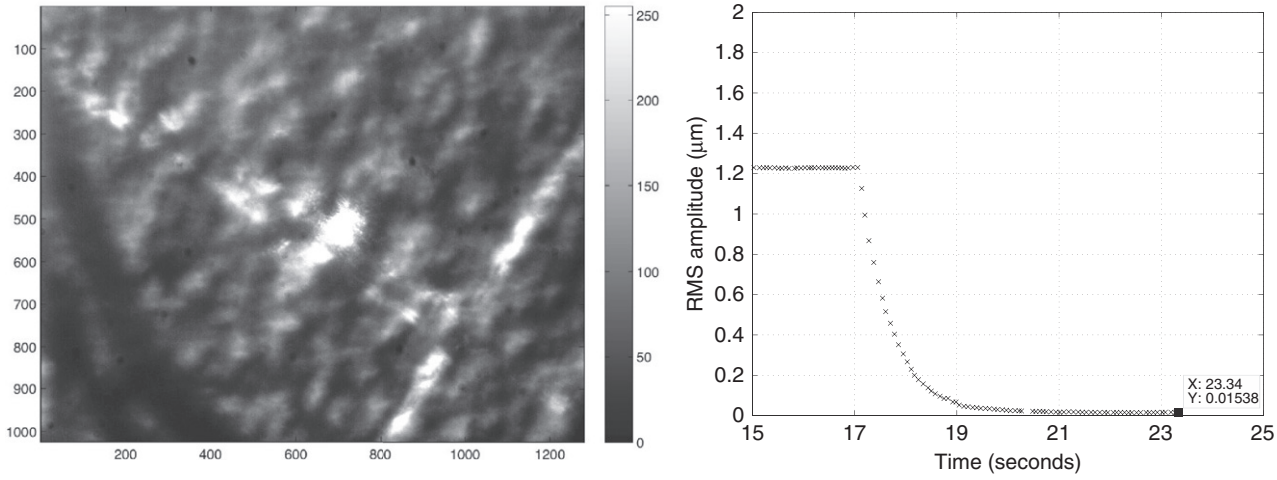

Figure 12. Imaging in the RUBR-EYE with adaptive optics at 100 ms and wavefront root mean squared error decrease from 1.2 μm to 0.015 μm before and after correction.

crosshairs at the image plane a magnification factor of 6× between the object and image plane was identified.

Adaptive optics applied to the RUBR-EYE presented in Figure 12(right) gave a final wavefront root mean squared correction of 0.015 μm using the parameters previously mentioned and a probe beam system based on a collimated beam of corrected tip–tilt inclination at the pupil. Imaging of the inside structure of the RUBR-EYE was realised with adaptive optics using the dynamic ranges 9, 15, 21 and 27 λ/D and sensor pupil samplings 110, 220, 330 and 440 μm per sample. Wavefront reconstruction of the aberration was dominated by defocus ($j=4$ term). An increase in the rms error with an increase in dynamic range was observed, possibly due to saturation of the sensor by defocus. Figure 13 shows that a constant image quality is obtained at a given depth with the change in the sensor settings, based on the visual definition of the background structure. The whiter shape on the lower-left of the image corresponds to a vessel shape.

Downloaded by [National University of Ireland - Galway] at 00:54 14 September 2012

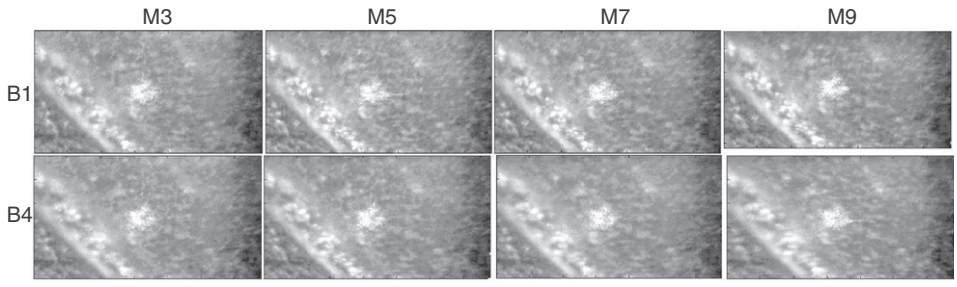

Figure 13. An increasing dynamic range (M3 = 9 λ/D to M9 = 15 λ/D from left to right) and two settings of pupil sampling (B1 = 110 μm/sample, top row and B4 = 430 μm/sample, lower row) after adaptive optics in RUBR-EYE at 50 ms camera exposure. The lack of visual variation in the definition of the background structure means independence towards the sensor parameters for this aberration.

Downloaded by [National University of Ireland - Galway] at 00:54 14 September 2012

This result is identified as representative of the independence of the adaptive optics performance towards these settings for the aberration corresponding to this object.

In conclusion, calibration of the imaging system resolution for objects imaged after correction of the system's static aberration and after correction of the aberration induced by a strong change in the refractive index has proved that the imaging with adaptive optics was efficient. In comparison to a model resolution defined by physical parameters the effective length and refractive index in the object from the pupil to the artificial retina determined the experimental magnification to the image plane.

5. Conclusion

In this paper, we have demonstrated the performance of a calibrated pyramid wavefront sensor used in ophthalmic applications, and its potential for use for retinal imaging in an adaptive optics configuration. Calibration of the sensor response to a quantified aberration and reconstruction in terms of Zernike polynomials has been presented for both low and high order aberrations, respectively, using ophthalmic lenses and custom-designed phase plates. Measurement and correction of the ocular aberration has been recorded using the probe beam signal as a fixation point. Calibration of the imaging system resolution has been defined mathematically and measured experimentally using resolution targets. Correction of a static aberration with imaging of the inside of the object was demonstrated using a custom-designed artificial eye.

Acknowledgements

We are grateful to Prof. S. Bará for providing the phase plates and to Dr E. Daly for the interferometric measurements. This research has been funded by the European Union under the FP6 funding Marie Curie Early Stage Training MEST CT-2005-020353 in the project 'Training in Methods and Devices for Non-invasive HIgh REsolution Optical Measurements and Imaging' (HIRESOMI) and by the Science Foundation Ireland SFI under Grant No. 07/IN.1/I906.

References

[1] Ragazzoni, R. *J. Mod. Opt*. **1996,** *43,* 289–293.
[2] Iglesias, I.; Ragazzoni, R.; Julien, Y.; Artal, P. *Opt. Express* **2002,** *10,* 419–428.
[3] Chamot, S.R.; Dainty, C.; Esposito, S. *Opt. Express* **2006,** *14,* 518–526.
[4] Chamot, S.R.; Esposito, S.; Dainty, J.C. Application of Pyramid Wavefront Sensing to Ocular Aberration Measurements and Corrections. In *Frontiers in Optics*, OSA Technical Digest Series; Optical Society of America, 2005; Paper FThZ3. http://www.opticsinfobase.org/abstract.cfm?URI = FiO-2005-FThZ3.
[5] Chiesa, S.; Daly, E.; Dainty, J.C.; Chamot, S.R. Adaptive optics system for retinal imaging based on a pyramid wavefront sensor. In *Adaptive Optics for Industry and Medicine*, Galway, Ireland, June, 2008; Dainty, J.C. Ed; Imperial College Press, 2008; Chapter 4, pp 336–341.
[6] Daly, E.M.; Dainty, J.C. *Proc. SPIE Opt. Sens. Detect*. **2010,** *7726,* 7760W.
[7] Daly, E.M.; Dainty, J.C. *Appl. Opt*. **2010,** *49,* G67–G77.
[8] Moreno-Barriuso, E.; Navarro, R. *J. Opt. Soc. Am. A* **2000,** *17,* 974–985.
[9] Cheng, X.; Himebaugh, N.L.; Kollbaum, P.S.; Thibos, L.N.; Bradley, A. *Optom. Vision Sci*. **2003,** *80,* 587–595.
[10] Wei, X.; Thibos, L. *Opt. Express* **2010,** *18,* 1134–1143.
[11] Diaz-Santana, L.; Dainty, J.C. *J. Opt. Soc. Am. A*. **2001,** *18,* 1437–1444.
[12] Dalimier, E. Adaptive Optics Correction of Ocular Higher-Order Aberrations and the Effects on Functional Vision. Ph.D. Thesis, Department of Experimental Physics, National University of Ireland, Galway, 2007.

[13] Devaney, N.; Dalimier, E.; Farrell, T.; Coburn, D.; Mackey, R.; Mackey, D.; Laurent, F.; Daly, E.; Dainty, C. *Appl. Opt*. **2008,** *47,* 6550–6562.
[14] Feeney, O.A. Theory and Laboratory Characterization of Novel Wavefront Sensor for Adaptive Optics Systems. Ph.D. thesis, National University of Ireland, Galway, 2001.
[15] Noll, R.J. *J. Opt. Soc. Am.* **1976,** *66,* 207–211.
[16] Thibos, L.N.; Applegate, R.A.; Schwiegerling, J.T.; Webb, R.; VSIA Standards Taskforce Members. *OSA TOPS* **2000,** *35,* 232–244.
[17] American National Standards Institute (ANSI). *American National Standard for Ophthalmics – Methods for Reporting Optical Aberrations of Eyes*; ANSI Z80. 28:2004 2007.
[18] Schwiegerling, J. *Field Guide to Visual and Ophthalmic Optics*; SPIE Press: Field Guides, 2004.
[19] Navarro, R.; Moreno-Barriuso, E.; Bará, S.; Mancebo, T. *Opt. Lett*. **2000,** *25,* 236–238.
[20] Leroux, C.E.; Tzschachmann, A.; Dainty, J.C. *Opt. Express* **2010,** *18,* 21567–21572.

Downloaded by [National University of Ireland - Galway] at 00:54 14 September 2012